

Article

Spaceborne Mine Waste Mineralogy Monitoring in South Africa, Applications for Modern Push-Broom Missions: Hyperion/OLI and EnMAP/Sentinel-2

Christian Mielke ^{1,2,*}, Nina Kristine Boesche ^{1,2}, Christian Rogass ¹, Hermann Kaufmann ¹, Christoph Gauert ³ and Maarten de Wit ⁴

¹ Helmholtz Centre Potsdam, German Research Centre for Geosciences, Telegrafenberg, 14473 Potsdam, Germany; E-Mails: nina.boesche@gfz-potsdam.de (N.K.B.); christian.rogass@gfz-potsdam.de (C.R.); hermann.kaufmann@gfz-potsdam.de (H.K.)

² Institut für Erd- und Umweltwissenschaften, Universität Potsdam, 14476 Potsdam, Germany

³ Department of Geology, University of the Free State (UFS), Bloemfontein 9300, South Africa; E-Mail: gauertcdk@ufs.ac.za

⁴ Africa Earth Observatory Network (AEON), Nelson Mandela Metropolitan University, Summerstrand, Port Elizabeth 6031, South Africa; E-Mail: maarten.dewit@nmmu.ac.za

* Author to whom correspondence should be addressed; E-Mail: christian.mielke@gfz-potsdam.de; Tel.: +49-331-288-1763; Fax: +49-331-288-1192.

Received: 7 March 2014; in revised form: 15 July 2014 / Accepted: 18 July 2014 /

Published: 25 July 2014

Abstract: Remote sensing analysis is a crucial tool for monitoring the extent of mine waste surfaces and their mineralogy in countries with a long mining history, such as South Africa, where gold and platinum have been produced for over 90 years. These mine waste sites have the potential to contain problematic trace element species (e.g., U, Pb, Cr). In our research, we aim to combine the mapping and monitoring capacities of multispectral and hyperspectral spaceborne sensors. This is done to assess the potential of existing multispectral and hyperspectral spaceborne sensors (OLI and Hyperion) and future missions, such as Sentinel-2 and EnMAP (Environmental Mapping and Analysis Program), for mapping the spatial extent of these mine waste surfaces. For this task we propose a new index, termed the iron feature depth (IFD), derived from Landsat-8 OLI data to map the 900-nm absorption feature as a potential proxy for monitoring the spatial extent of mine waste. OLI was chosen, because it represents the most suitable sensor to map the IFD over large areas in a multi-temporal manner due to its spectral band layout; its (183 km × 170 km) scene size and its revisiting time of 16 days. The IFD is in good agreement with primary

and secondary iron-bearing minerals mapped by the Material Identification and Characterization Algorithm (MICA) from EO-1 Hyperion data and illustrates that a combination of hyperspectral data (EnMAP) for mineral identification with multispectral data (Sentinel-2) for repetitive area-wide mapping and monitoring of the IFD as mine waste proxy is a promising application for future spaceborne sensors. A maximum, absolute model error is used to assess the ability of existing and future multispectral sensors to characterize mine waste via its 900-nm iron absorption feature. The following sensor-signal similarity ranking can be established for spectra from gold mining material: EnMAP 100% similarity to the reference, ALI 97.5%, Sentinel-2 97%, OLI and ASTER 95% and ETM+ 91% similarity.

Keywords: mine waste; spatial extent; gold; platinum; South Africa; EnMAP; OLI; Hyperion; Sentinel-2; iron feature depth (IFD)

1. Introduction

Mapping and monitoring mine waste has been identified as a crucial application in the field of imaging spectroscopy and remote sensing. Numerous studies employ airborne imaging spectroscopy data [1–3] to map potential areas of acid mine drainage (AMD) generation, taking advantage of the abundance of specific secondary iron minerals that are stable in a specific pH range, indicating AMD generating conditions [1].

The formation of AMD results from the oxidation of sulfides under environmental conditions that promote the contact of water and oxygen with the mine waste material. This produces acid and ferrous iron [1–3]. Secondary iron minerals that are generated during this process and that can be discriminated by spectroscopy are jarosite, ferrihydrite, goethite and copiapite, for example [1,2]. This enables qualitative mapping of zones of potential AMD generation and provides a semi-quantitative measure for the magnitude of pollution in a specific area [1]. AMD is in this regard a challenging problem, because it can mobilize potentially problematic trace elements from tailings disposal sites, such as uranium, chromium, arsenic, copper and lead, amongst others.

Most AMD work to date has focused on well-studied mining sites in highly industrialized countries, such as, e.g., the United States of America [1], Spain [4], Germany [5], Czech Republic [6,7], Canada [8], Hungary [9] and Australia [10]. All of these aforementioned studies employed airborne hyperspectral data as the main source of imaging spectroscopic data in their work, except for [3], which also employed spaceborne hyperspectral data in their work of characterizing mine waste. Of these studies, the studies in Germany [5] and the Czech Republic [6,7] focused on acid mine drainage generation and the pH regime in coal mining; whilst the studies in the USA [1], Spain [4], Canada [7] and Hungary [9] deal with mine waste from precious and base metal mining. Out of these studies, especially the studies in Spain [4] and Hungary [5] additionally deal with mapping the distribution of problematic trace elements.

Due to the high costs and difficult logistics involved in monitoring mine waste areas, only limited remote sensing and imaging spectroscopy have been carried out in developing countries. In this

context, South Africa is a prime example. Here, large regions have been affected by mining operations and the related disposal of environmentally problematic tailings material, as well as AMD generation from past and present mining activity. This issue has been identified as one of the major challenges for sustainable living [11,12]. This topic has been addressed by the Mineo Project [5] and the recent EO-Miners initiative, a European Union project that aims to monitor the impact of mining on environment and society, at regional spatial scales using imaging spectroscopic methods, as reported, e.g., by Kopačková in [6] and [7] in the Czech Republic and in South Africa [13], to provide a first order rapid environmental assessment of areas affected by mining. The last named study, however, primarily focuses on coal mining activity in the eMalahleni area of Mpumalanga, South Africa, using focused airborne hyperspectral data, [13] and excludes comprehensive monitoring of large-scale tailings sites from the precious- and base-metal mining activities.

Therefore, airborne image spectroscopy data is not suitable for cost-effective, repetitive mineral mapping and determination of the areal extent of mine waste surfaces.

Rapid, efficient and spatially extensive mapping and monitoring of mining activities and waste accumulation around tailings areas can only be achieved through a combination of multispectral and hyperspectral spaceborne sensors. Here, we present analyses based on current hyperspectral sensors (EO-1 Hyperion [14]) and multispectral sensors (Landsat 7 ETM+ [15], EO-1 ALI [14] and Landsat 8 OLI [16]), from the National Aeronautics and Space Administration (NASA), which are available free of charge. Although ETM+ is a whisk-broom scanner, we include it in our analysis for the sake of completeness. These systems will be supplemented by the next generation instruments, EnMAP [17] (Environmental Mapping and Analysis Program) and Sentinel-2 [18], with a similar data-use policy.

The aim of this paper is to explore the potential of spaceborne imaging spectrometers, such as Hyperion, to map and monitor the spatial extent of mine waste surface material in areas with mine tailings and to find common links between hyperspectral and multispectral systems, such as the Landsat program or the next generation Sentinel program of the European Space Agency (ESA), both designed as mapping missions. This common link might then be exploited for mapping and monitoring the spatial extent of surfaces affected by mine waste. We specifically focus on how sensor-specific parameters (e.g., center wavelength and band pass) influence the ability to discriminate mine waste surfaces from their surroundings.

South Africa, with a mining history of more than hundred years, provides an excellent platform for the application of spaceborne hyperspectral and multispectral sensors for the monitoring of mine waste sites and tailings facilities.

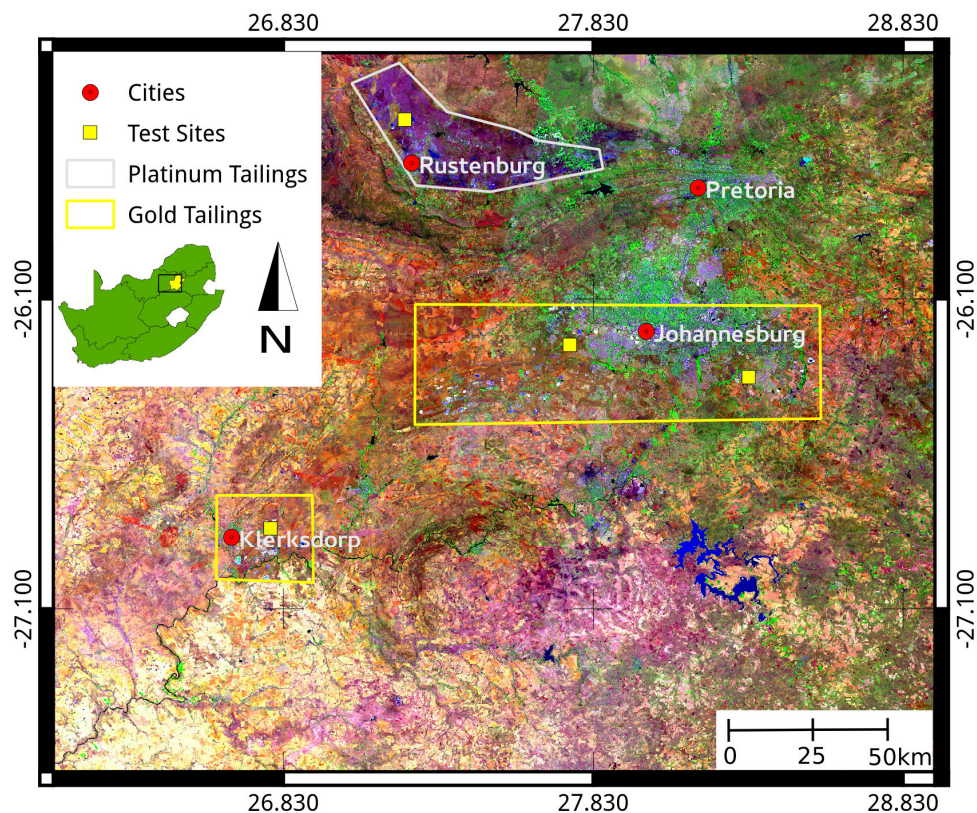
The main link between multispectral and hyperspectral data can be established by utilizing absorption features. Those have to be spectrally broad enough to be present in both multispectral and hyperspectral data. Additionally, they must be diagnostic for primary and secondary iron-bearing minerals that are characteristic for mine waste sites from platinum and gold mining. These minerals are listed in Table 1 of the Supplementary Material. The characteristic absorption features of iron-bearing minerals are based on the fact that ferrous iron in minerals shows a distinct characteristic absorption feature around 900 nm [19,20], which has been attributed to crystal field transitions in ferrous iron [19]. In addition to that, prominent secondary iron minerals, such as goethite, hematite and jarosite, are characterized by a reflectance minimum centered around 900 nm [2,20,21]. This absorption feature has already been described by Hunt and Ashley [22] to occur between 750 nm and

910 nm, with 750 nm being the left shoulder of this feature. These secondary iron-bearing minerals are also associated with mine waste areas and acid mine drainage generation [1,2].

2. Study Area

We focused our work on mining activities associated with the two most prominent mineral commodities in South Africa, namely gold from the Witwatersrand Basin and platinum group elements (PGEs) from the layered mafic intrusion (LMI) of the Bushveld Complex, as shown in Figure 1.

Figure 1. Landsat 8 composite (R: 2200 nm, G: 860 nm, B: 550 nm) showing the tailings facilities visited for this study (yellow stars). The yellow province in the inset map is Gauteng; the black box shows the boundaries of the study area. Note the extent of the Bushveld layered mafic intrusion (LMI), which can be distinguished by its dark soils.



2.1. Geological Background

Gold was mined for more than one hundred years from the rocks of the West Rand Group (2.97–2.91 Ga) and to a greater extent from the rocks of the Central Rand Group (2.89–2.71 Ga) [23], which together constitute the Archean Witwatersrand Supergroup dated between 3.07–2.7 Ga [24]. The detrital and remobilized gold occur predominantly in pyrite, together with a significant amount of uranium ore as uraninite. These minerals are hosted in coarse-grained quartzites and conglomerate “reefs” [23].

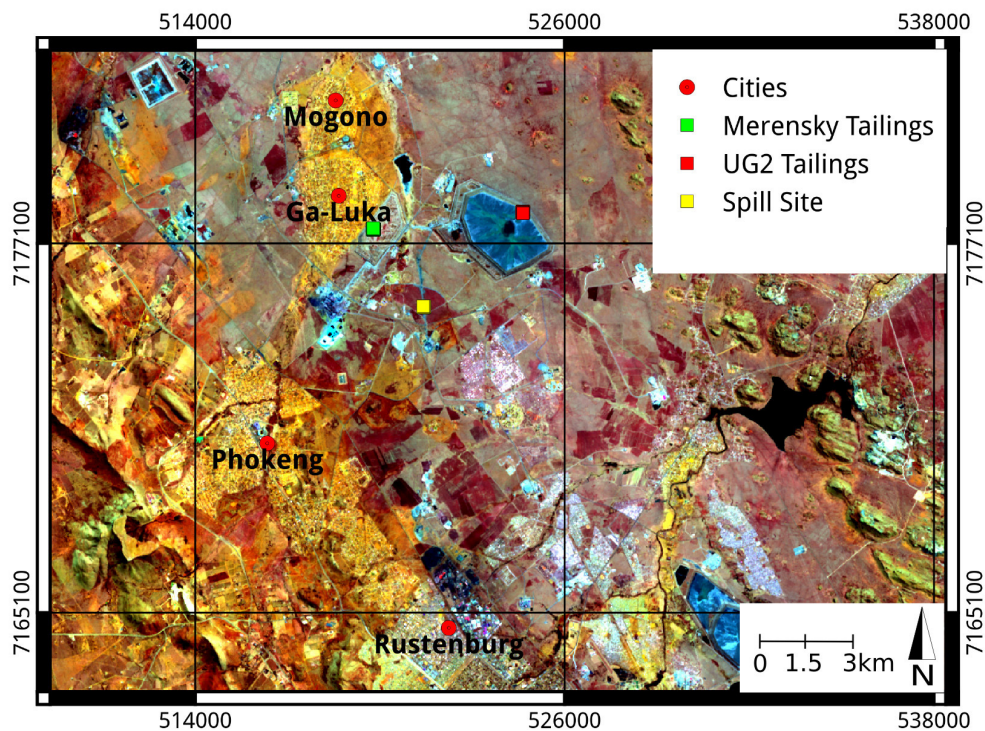
For our gold-related studies, we visited the Brakpan Tailings Facility near Benoni (Johannesburg) and the tailings facility near Stilfontein (Klerksdorp) to conduct *in situ* field-spectrometer measurements and sample collection.

Platinum in South Africa is mined from two important horizons in the ultramafic Bushveld Complex with its main magmatic phase dated at 2.054–2.061 Ga [25]. The most important economic horizons of the Bushveld Complex are the Merensky Reef (2054.4 ± 1.3 Ma) [25], where sulfides containing PGE are hosted in a coarse-grained orthopyroxenite rock [25]. The stratigraphically lower Upper Group 2 (UG2) pyroxenite (~2042 Ma) hosts sulfides that are PGE bearing in chromitite layers [26]. Our study investigated tailings dams from both the Merensky Reef and the UG2 pyroxenite and chromitite strata near GaLuka (Rustenburg), for *in situ* field-spectrometer measurements and sample collection (as shown in Figure 1).

2.2. Platinum Tailings near Rustenburg

The field sites in Rustenburg are comprised of three test sites in the area of the Impala tailings operations sites, shown in Figure 2. The first site is the large active tailings facility that is built of UG2 waste rock material. The second site is a tailings dam to the southeast of Ga-Luka. In 1974, the then active Merensky Tailings Dam experienced a major wall failure [27]. This event caused the outflow of 13 million m³ of tailings material [27]. Today, this tailings site has been reclaimed. Most of the tailings dam is covered by grass, shrubs and trees. The spill site represents an area next to an overpressure valve along the street. Here, tailings material had recently been deposited. At all three sites, 17 test surfaces were measured and sampled according to the sampling scheme described in the Methodology Section.

Figure 2. Landsat 8 composite (R: 2200 nm, G: 655 nm, B: 482 nm) showing the tailings facilities and test sites (colored stars) visited in the field area near Rustenburg.

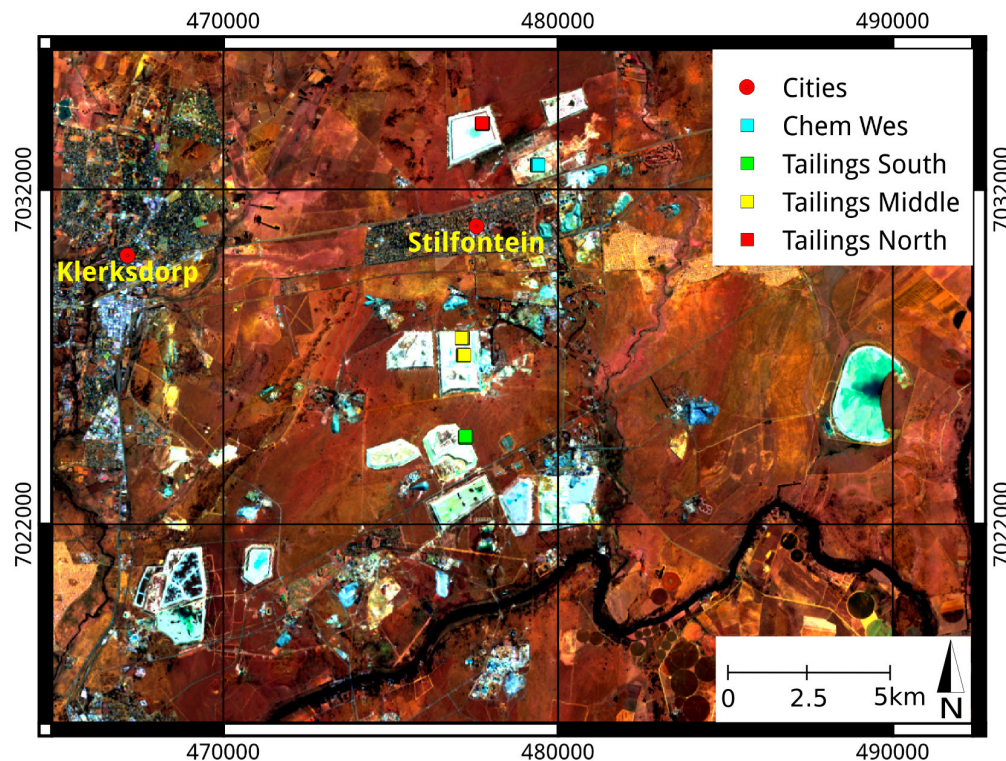


A potential problematic environmental feature is the abundance of chromitite in the tailings material and its spatial distribution in the areas adjacent to the tailings dams, as these areas are used for informal livestock grazing of the neighboring communities, such as GaLuka. Sulfides are not part of the tailings material. AMD is therefore no problem in this area.

2.3. Gold Tailings near Stilfontein

The gold tailings to the north and south of Stilfontein are comprised of active, reclaimed tailings and tailings sites, which are currently being reprocessed to recover additional gold. The Chem Wes site represents the footprint of an already reprocessed tailings dam. Here, a blanket of up to five centimeters of tailings material covers the original surface. “Tailings North” represents the youngest tailings site of the visited field sites in Stilfontein. “Tailings Middle” was being prepared for reprocessing during the time of our fieldwork. “Tailings South” is under active re-mining and represents the oldest tailings site of all of the visited tailings sites. Figure 3 shows the dynamic tailings landscape around Stilfontein, where the reprocessed material of the old dams acts as feeder material for the new tailings site in the east. At all five field sites, 17 test surfaces were measured and sampled according to the scheme described in the Methodology Section. The potential of generating AMD here is largely controlled by the sulfide content in the tailings, which depends on the mineral processing techniques used (changes in milling technology) [28]. In addition to that, the price of the secondary commodity sulfuric acid determines if sulfides were extracted or not [28].

Figure 3. Landsat 8 composite (R: 2200 nm, G: 655 nm, B: 482 nm) showing the tailings facilities and test sites (colored stars) visited in the field area around Stilfontein.



3. Fieldwork

A matrix grid representing 3×3 Hyperion pixels was laid out at each of the test sites described above, which represents an area of 90×90 m. This spatial scale also coincides with the spatial resolution of EnMAP, ALI and OLI. Only test sites that were homogeneous enough on this spatial scale were considered as test sites; sites with notable vegetation cover were thus avoided as far as possible. Seventeen test surfaces of one square meter each [29] were measured per test site using an ASD Fieldspec Pro with a large contact probe with a field of view of 2 cm, due to unfavorable weather conditions. Five spectra were acquired per test surface, resulting in 85 spectra per test site. The five spectra of each site are averaged in order to produce a representative average test spectrum for each of the 17 test surfaces. A sketch of the sample layout is shown in the Supplementary Materials. Surface samples of the test surfaces were collected for XRD, XRF and laboratory spectroscopy by scraping off the surface with a small stainless steel shovel after the spectral measurements. The outermost test surfaces represent the centers of the eight neighbor pixels, whilst the nine innermost test surfaces include the center of the central pixel and its immediate surroundings of test surfaces, halfway towards central pixel edges, as shown in Supplementary Figure S1. This specific sampling strategy was chosen, because it simulates the point spread function of the spaceborne sensor, in our case, Hyperion and EnMAP. A synthetic EnMAP or Hyperion pixel spectrum was generated by Gaussian weighting of the 17 test surface spectra. The field samples were analyzed by X-ray diffraction (XRD) (Empyrean from PANalytical) and X-ray fluorescence analysis (XRF) (Axios WD from PANalytical) at the University of the Free State (UFS) in South Africa.

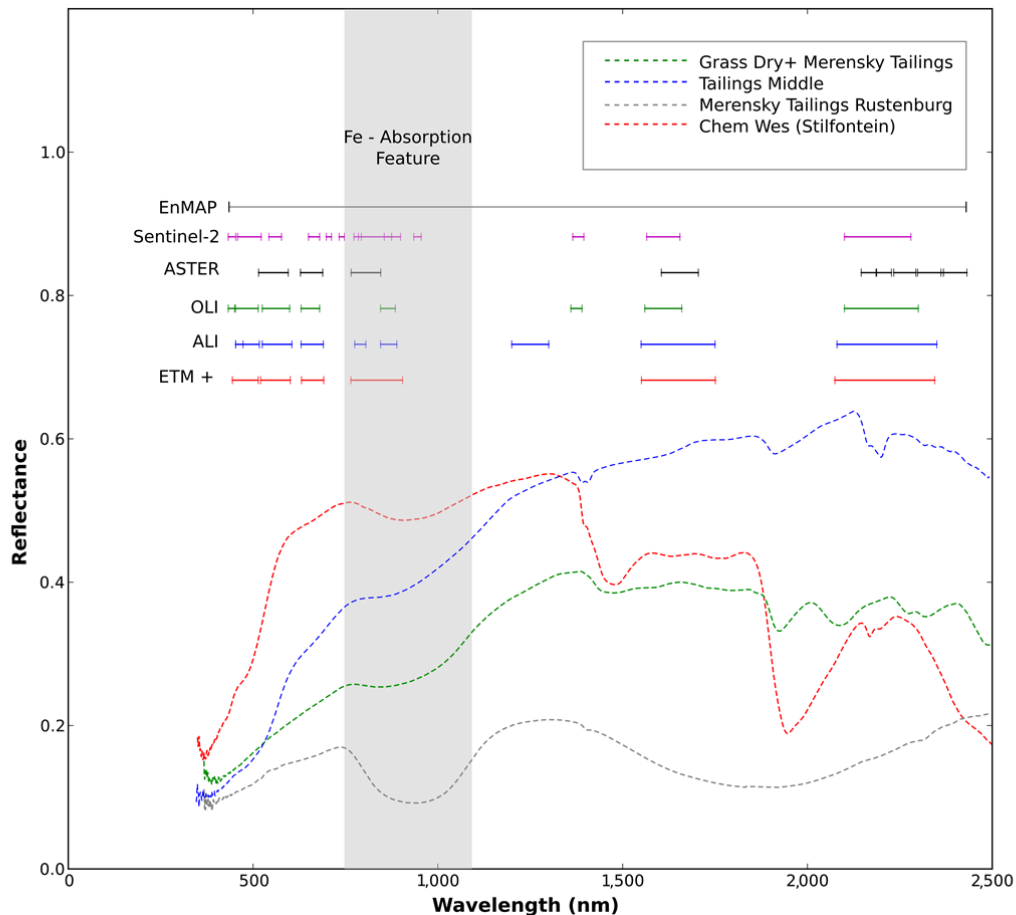
4. Methodology

The large iron absorption feature around 900 nm (± 40 nm potential bias) [20–22] can serve as a common link between hyperspectral and multispectral data, because it is wide enough and can be detected by both multispectral and hyperspectral instruments, as shown in Figure 4. The shoulders of this absorption band to the shorter wavelength side are located at 750 nm, as stated in [22]. The right shoulder of this absorption feature is best placed outside of the atmospheric water absorption bands at 940 nm, 1130 nm and 1380 nm. We therefore propose to place the right shoulder of the iron feature at 1250 nm to avoid these absorption bands. This absorption feature is utilized in the following to map the spatial extent of this iron feature using multispectral data, from NASA's OLI, and through this, delineate areas affected by mine waste cover. The resulting spatial extent is compared with mineral mapping results from the spaceborne hyperspectral sensor, Hyperion, for iron mineral characterization and validation.

4.1. Preprocessing of Multispectral Spaceborne Data

Multispectral data has long been used to delineate and map different surface cover types in earth science through band ratios [30,31]. Therefore, they represent the first starting point in the search for methods to delineate and map mine waste surfaces from multispectral spaceborne data. Band ratios also have the advantage that a top of the atmosphere reflectance (TOAREF) may be sufficient to yield indices that are atmospherically stable enough for delineating the spatial extent of mine waste sites.

Figure 4. Band positions of selected multispectral sensor systems overlain on field spectra from the mine waste sites in South Africa. Continuous data coverage of EnMAP are shown for reference. Note the position of the near-infrared channels of the multispectral sensor systems within the broad iron absorption feature at 900 nm.



Therefore, band ratios were calculated as the first step in the analysis of the multispectral data from ALI, ETM+ and OLI, according to Table 1, which were compiled from [32]. This was performed for the TOAREF and at-ground-reflectance (shortly reflectance) data for each of the three sensors over the Stilfontein tailings site. Reflectance data was calculated from sensor radiance using the ATCOR 2/3 software package [33]. After that, the mean structural similarity index measure (MSSIM) from Wang *et al.* [34], implemented in scikit-image [35], was calculated for each corresponding TOAREF/reflectance pair, as shown in Table 1, according to the processing scheme and equations in the Supplementary Materials. Table 1 clearly shows that, despite ALI, due to the small scene size, the deviations (1-MSSI) are mainly >60%. This implies that a conversion to TOAREF is not reliable for the calculation of atmospherically-insensitive indices. For this reason, and to enable comparability between different sensors, only reflectance data was further considered.

The further use of spectral indices for a spatial delineation of mine waste surfaces is, however, problematic, because these indices may not necessarily characterize physical absorption features well enough [36]. Here, it was shown that a simple three-point band depth may aid the discrimination of mineral cover types better than simple band ratios [36].

Table 1. Selected ratios that indicate ferric/ferrous iron, gossan and ferric silicates and the mean structural similarity index measure (MSSIM) between each ratio calculated from top at the atmosphere reflectance (TOAREF) data and reflectance data. The naming convention of the spectral bands in the formulas: near-infrared (NIR) in this case is the sensor band closest to 900 nm, whilst short wave infrared 1 (SWIR1) is the band closest to 1600 nm and short wave infrared 2 (SWIR2) is the last band of ALI, ETM+ and OLI. (-) shows that the calculation of 1-MSSIM was not possible in two cases, due to absence of data values in the ratio data. The smaller the 1-MSSIM values, the better the result.

Index Name	Formula	(1-MSSIM ETM+)	(1-MSSIM) ALI	(1-MSSIM OLI)	Ref.
Ferric Iron	$\frac{SWIR2}{NIR} + \frac{RED}{GREEN}$	0.702	0.009	0.695	[37]
Ferric Iron_n	$\frac{(SWIR2 - NIR)}{(SWIR2 + NIR)} + \frac{(RED - GREEN)}{(RED + GREEN)}$	0.645	0.201	(-)	[37]
Ferric Oxides	$\frac{SWIR1}{NIR}$	0.692	0.003	0.686	[38]
Ferric Oxides_n	$\frac{(SWIR1 - NIR)}{(SWIR1 + NIR)}$	0.64	0.251	0.767	[38]
Ferric Silicates	$\frac{SWIR2}{NIR}$	0.145	0.003	0.67	[38]
Ferric Silicates_n	$\frac{(SWIR2 - NIR)}{(SWIR2 + NIR)}$	0.668	0.091	(-)	[38]
Gossan	$\frac{SWIR1}{RED}$	0.603	0.47	0.539	[39]
Gossan_n	$\frac{(SWIR1 - RED)}{(SWIR1 + RED)}$	0.682	0.096	0.785	[39]
NDVI	$\frac{(NIR - RED)}{(NIR + RED)}$	0.013	0.026	0.871	[40]
Red_Blue_n	$\frac{(RED - BLUE)}{(RED + BLUE)}$	0.736	0.148	0.633	[31]

4.2. Preprocessing of Hyperspectral Spaceborne Data

Data from NASA's spaceborne EO-1 Hyperion imaging spectrometer are the only freely available source of hyperspectral data for all the studied tailings dam facilities. After correcting the vertical pixel shift in the SWIR detector, the spatial shift between the visible/near-infrared (VNIR) detector and the short wave infrared (SWIR) detector was corrected [41]. After that, the destriping method of Datt *et al.* [41] was applied in combination with the destriping routine of Staenz *et al.* [42]. This is necessary to reduce cross track striping in the image data, which impacts on succeeding analyses, like Material Identification and Characterization Algorithm (MICA) [43]. Atmospheric correction was carried out using the physics-based EnMAP atmospheric correction routine of Guanter and Rogass, which is part of the free and open source EnMAP Box software [44]. After that, the data are analyzed with the USGS MICA [43], which is able to map primary and secondary iron minerals on the surfaces of mine dumps and tailings, highlighting potentially polluted sites. MICA is based on the USGS material detection and mapping algorithm TETRACORDER that uses characteristic physical absorption features to identify surface materials, such as minerals, based on the position, shape and absorption depth of these absorption features [36].

4.3. Linking Multispectral and Hyperspectral Data through Laboratory Work

The surface samples were scanned with the HySpex [45] imaging spectrometer system in the spectral laboratory using the nadir view, with a distance of 1 m from the detector to the sample. The HySpex setup consists of a HySpex 1600 VNIR and a HySpex 320 m-e SWIR spectrometer with a 2000 W Hedler studio light as the light source. The samples are moved on a translation stage, enabling the fixed mounted line scan cameras of the HySpex system to acquire a full hyperspectral scene of the samples. Co-registration and reflectance retrieval from the HySpex data is done with an in-house Interactive Data Language routine that basically combines affine fast Fourier transform techniques [46] for image registration and manual delineation of the reflectance panel for irradiance normalization and reflectance retrieval. With this technique, we were able to collect a scene with 50×50 pixel spectra, resulting in 2500 spectra per surface sample at 1-m distance. The individual HySpex sample images were spectrally resampled to the resolution of the following multispectral sensors: (Advanced Land Imager, Operational Land Imager, ETM+, Sentinel-2 and the Advanced Spaceborne Thermal Emission and Reflection Radiometer (ASTER) [47]) using a customized code adopted from Spectral Python (SPY) [48] that generates the according channel filter files from the center wavelengths and the full width at half maximum values to resample a given high resolution spectrum to a sensor with lower spectral resolution (e.g., resampling HySpex to OLI) using Gaussian filter functions that approximate unavailable spectral response functions (SRF). Although, this is a broadly used technique, full end to end sensor simulations (EeteS simulations [49]) were not possible, due to unavailable airborne hyperspectral data over the study areas.

The images were again resampled to a generic 1-nm sensor together with the original HySpex data, using cubic splines [50], to ensure the comparability for the following tests incorporating the same band positions. The mean structural similarity index measure (MSSIM) from Wang *et al.* [34], implemented in scikit-image [35], was calculated between each generically resampled multispectral sensor image and the generically resampled HySpex reference. The MSSIM was selected as a quality indicator, because it represents a sensitive image-based measure to detect subtle changes between similar images, such as image noise, contrast and brightness changes, which can be induced by spectral resampling and interpolation. The method and the processing workflow are illustrated in the Supplementary Materials. This was done in the spectral regions, bounded by the left and right shoulders of the maximum absorption of the iron absorption features near 900 nm, as listed in Supplementary Table 1. Here, the feature definitions are after the USGS TETRACORDER Database [36] and the USGS digital spectral library [51], whilst the formulas follow after [52]. These spectra were chosen, because they represent the three main groups that are of interest in this study: iron oxides (from the oxidation of iron-bearing minerals), mine waste (reference spectra related to the generation of acid mine drainage) and pyroxenes (important rock-forming minerals in the mafic intrusives of the Bushveld LMI that can be detected in the VNIR by imaging spectroscopy). The characteristic absorption features of primary and secondary iron minerals around 900 nm (± 40 nm potential bias) listed in Table 1 of the Supplement Materials were chosen as the basis for the sensor comparison.

The spectral range and the spectral contrast of this iron absorption feature enables the detection of iron-rich minerals on mineral waste surfaces that could indicate acid rock drainage generation [2].

To be able to assess the theoretical potential to resolve this iron absorption feature, the MSSIM [34] and (e_m), mean model error (Equation (1)), were computed as:

$$e_m = \frac{\sum_n \frac{r_{sensor} - r_{HySpex}}{r_{HySpex}}}{n} \quad (1)$$

where e_m denotes the mean model error (MME), n the number of samples, r_{sensor} the reflectance spectra simulated for a specific sensor and r_{HySpex} the reflectance spectra acquired by HySpex.

Figure 5a shows an example for data from the Merensky Reef tailings site in Rustenburg, where the deviation in the MSSIM is low (<10%) for OLI, ALI and Sentinel-2. The deviations for ASTER and ETM+ are, however, >10%, especially for the pyroxenes from feature Number 14 onward, which represent a major component of the Merensky tailings material. The MME shows deviations of *ca.* 18% for ASTER and deviations above 20% for ETM+. Figure 5b shows a similar image, where data from the Chem Wes tailings site is plotted. Note that the feature numbers up to 14 represent secondary iron minerals. ETM+ again shows the largest deviation, with an average error of 8%, followed by ASTER and OLI. This shows that OLI with its continuous multi-temporal coverage is a multispectral sensor that can significantly contribute to mapping and monitoring of the spatial extent of mine waste surfaces, which contain primary and secondary iron-bearing minerals. OLI data shows, in this respect, better performance than the multispectral sensors, ASTER or ETM+.

To exploit this ability for mapping the areal extent of mine waste via the 900-nm iron absorption feature, we propose the iron feature depth (IFD) as the difference between the reflectance (r) in the near-infrared channel closest to 900 nm ($r(NIR)$) and the linearly interpolated reflectance value ($r_{int}(NIR)$); see Equation (2). $r_{int}(NIR)$ is calculated according to Equation (3), where $r(RED)$ denotes the reflectance of the sensor channel closest to 750 nm and $r(SWIR1)$ denotes the short wave infrared 1 channel, SWIR1, closest to 1250 nm. Channels that are specifically placed in, or near to, water vapor absorption bands, such as channels for cirrus cloud detection, e.g., OLI band No. 9 or Sentinel-2 band No. 10, are not taken into account for the calculation of $r(NIR)$, due to their low reflectance values. The difference between the interpolated value, ($r_{int}(NIR)$) and ($r(NIR)$) gives the IFD.

In the case of the OLI sensor, $r(NIR)$ is the reflectance of the near-infrared band at 865 nm (Number 5), $r(SWIR1)$ is the reflectance of the SWIR1 band (Number 6) at 1600 nm and $r(RED)$ is the reflectance of the red channel (Number 4) at 650 nm, as shown in Equation (4). The band numbers for OLI follow the definition given by [16].

$$IFD = r_{int}(NIR) - r(NIR) \quad (2)$$

$$r_{int}(NIR) = r(RED) + (r(SWIR1) - r(RED)) * \frac{\lambda NIR - \lambda RED}{\lambda SWIR1 - \lambda RED}$$

$$r_{int}(900 \text{ nm}) = r(750 \text{ nm}) + (r(1250 \text{ nm}) - r(750 \text{ nm})) * \frac{\lambda(900 \text{ nm}) - \lambda(750 \text{ nm})}{\lambda(1250 \text{ nm}) - \lambda(750 \text{ nm})} \quad (3)$$

$$r_{intOLI}(865 \text{ nm}) = r(650 \text{ nm}) + (r(1600 \text{ nm}) - r(650 \text{ nm})) * \frac{\lambda(865 \text{ nm}) - \lambda(650 \text{ nm})}{\lambda(1600 \text{ nm}) - \lambda(650 \text{ nm})} \quad (4)$$

Only positive values of the IFD are considered as a relevant indicator for iron absorption and, thus, the presence of iron-bearing minerals on the surface cover, as shown in Figure 6.

Figure 5. Band comparison of multispectral and hyperspectral sensors for sample spectra from the Merensky Reef mine waste site (a), shown directly below, and from spectra from the Chem Wes footprint mine waste site (b), shown below (a). Errors displayed were computed between the HySpex reference and the resampled multispectral sensors for the iron absorption features listed in Table S1. EnMAP with an offset of 0.01 is shown for reference purposes only. Note the large deviation of ETM+ (above 15%) and ASTER in the pyroxene region from mineral feature-number 14 (see Table S1) onwards as pyroxenes are a major component of the platinum group element (PGE)-bearing rocks (a). Large deviations are also found in ETM+ and ASTER in the region of secondary iron minerals up until 14 at the Chem Wes Site (b), as these minerals are indicative of acid rock drainage generation on tailings dam sites.

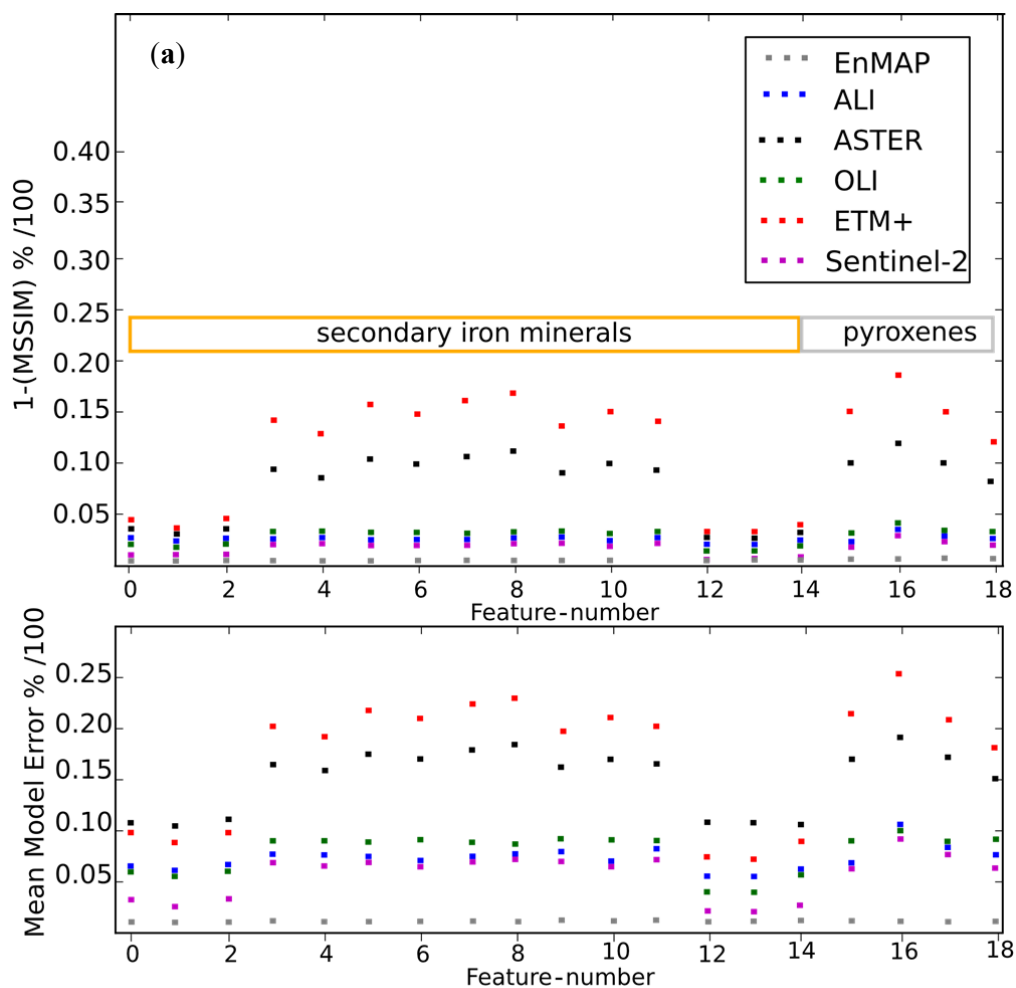


Figure 5. Cont.

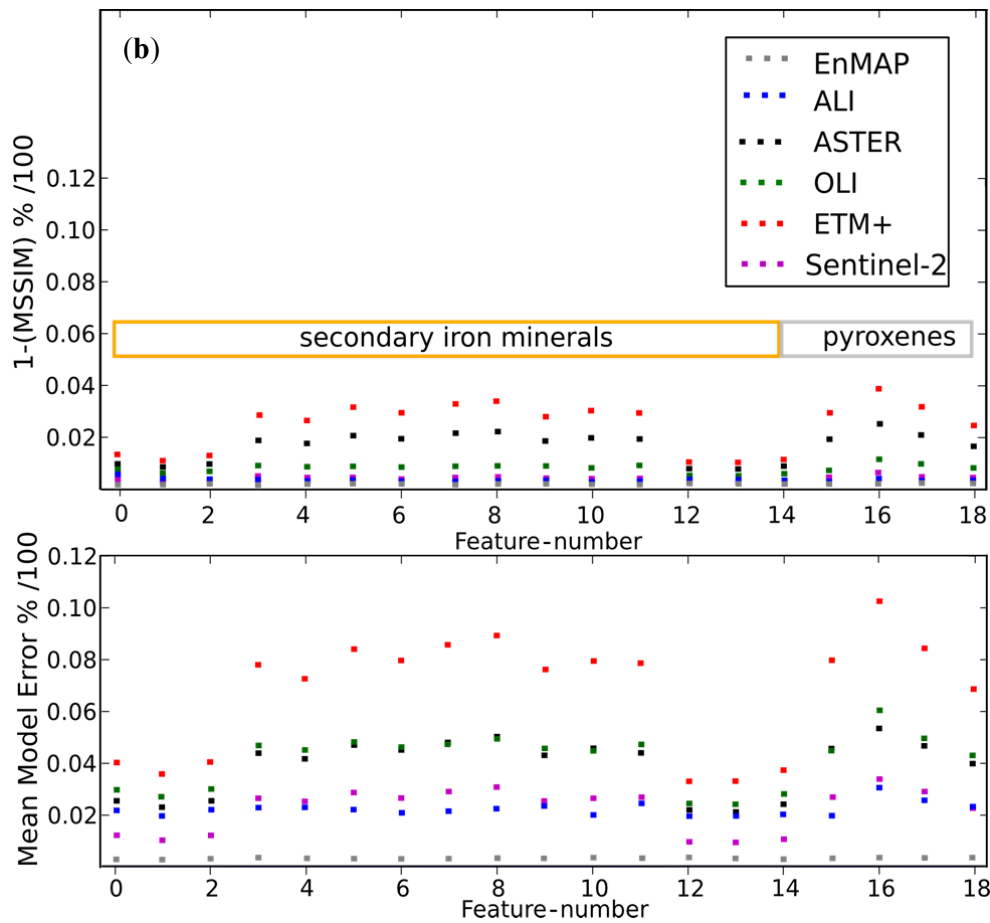
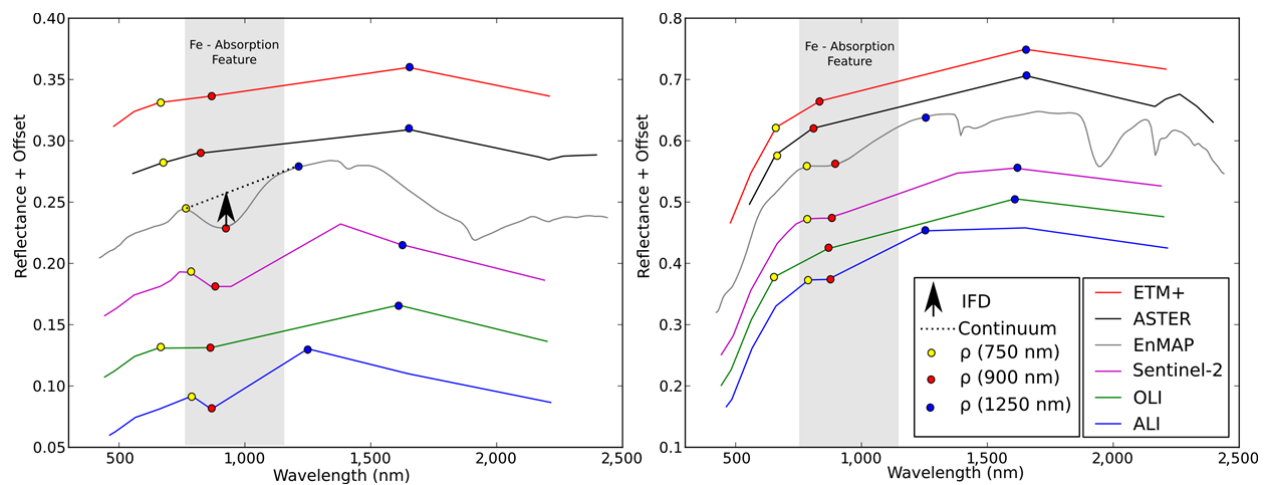


Figure 6. Spectra of multiple sensors generated from spectral resampling of the point spread function weighed field spectra from platinum mine tailings (left) and from mine waste associated with gold mining (right). Note that only EnMAP, Sentinel-2, ALI and OLI are able to spectrally resolve the iron absorption feature at 900 nm in the case of the material associated with platinum mining (left). The EnMAP reference spectrum is in grey at the original reflectance level; all other spectra are successively offset by 0.05 for clarity.



5. Results and Discussion

The analyses of the multispectral indices [32] from TOAREF data and reflectance data (Table 1) indicate that the process of ratio calculation benefits from atmospherically corrected data. This assumption can be confirmed by considering the large deviations of MSSIM values that have been calculated between the ratio images based on TOAREF and on atmospherically corrected data (reflectance). Values >0.65 here represent an error greater than 65%. However, ratios and indices are sufficient if a visual identification and enhancement of spectral gradients [32] in a multispectral dataset is the main goal [30]; however, this approach is therefore not sufficient for a robust and reproducible mapping result for the monitoring of the spatial extent of mine waste surfaces.

For a comparison with the results from hyperspectral data, a link between the main physical absorption feature of interest has been established, which is the iron absorption at 900 nm [19,21,22] in this case. Using this approach, physics-based absorption features [36,43] can be specifically adapted to be applicable to multispectral sensors. This link can be provided by the IFD, as illustrated in Figure 5a,b. Here, the sensor-dependent ability to map the iron feature is shown. Here, multispectral sensors, which have a favorable band characteristic to resolve the iron absorption feature (see Figures 4 and 6), show smaller errors in determining the shape of the iron absorption feature and, hence, the IFD. These sensors are, for example, Sentinel-2, ALI and OLI.

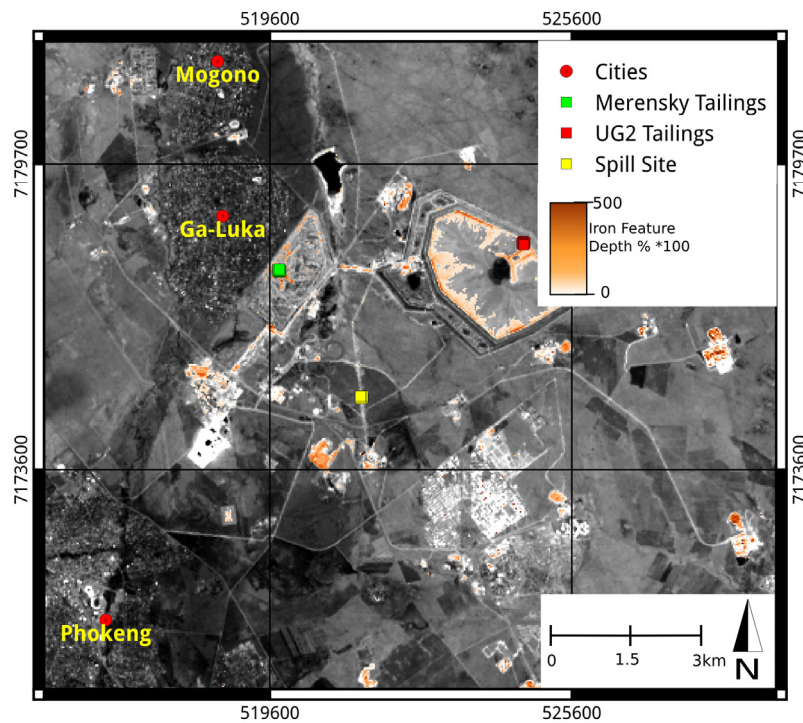
5.1. Results from Multispectral and Hyperspectral Spaceborne Data

Data from OLI was used for the calculation of the IFD over the Rustenburg, Figure 7a, and Stilfontein areas, Figure 8a. Additionally, data taken from the Hyperion instrument were analyzed with the USGS MICA algorithm [43] to map the spatial distribution of primary and secondary iron minerals in the mine waste areas of Rustenburg (Figure 7b) and Stilfontein (Figure 8b). Figure 7a,b shows a high coincidence between the abundance of iron-bearing minerals and their spatial extent and areas mapped with positive IFD. This shows that the IFD may be used as an indicator to map and monitor the spatial extent of mine waste from platinum mining. This is an important fact, because here, the pyroxenes may be used as a proxy for the presence of mine waste associated with platinum mining, as the XRD analysis in Table 2 by Reid [53] and the MICA analysis of field spectra show. In the case of the platinum tailings material, a high concentration of potentially problematic trace elements, such as chromium and nickel, as shown in Table 2, further motivates the monitoring of the spatial extent of platinum tailings material through spaceborne sensors. Here, the IFD could be used as a proxy for the presence of tailings material and, therefore, a potential proxy for problematic trace elements, such as chromium and nickel.

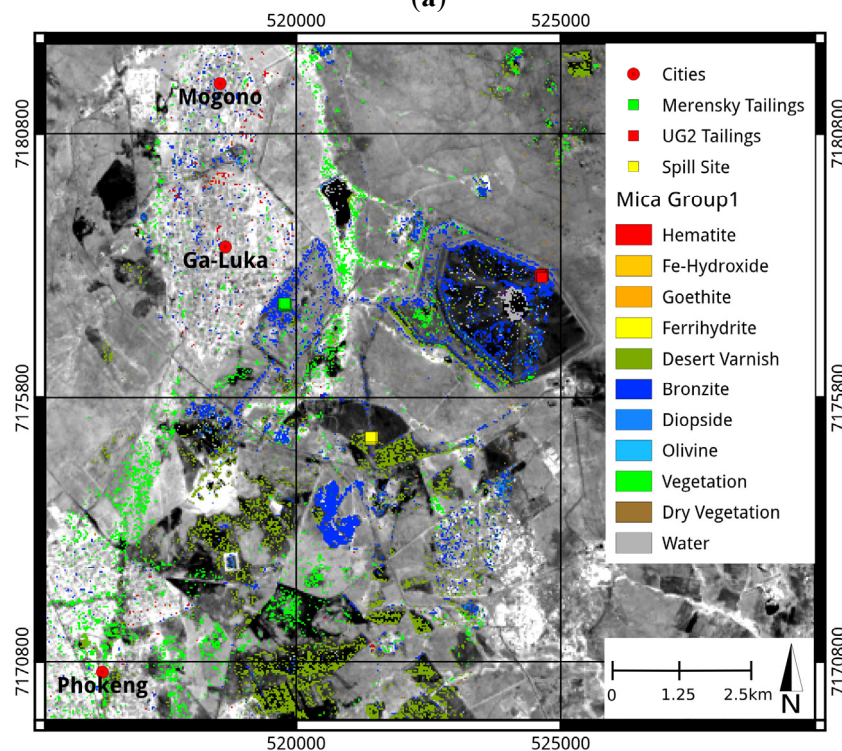
Table 2. Mineralogy derived from X-ray diffraction analysis (XRD) from the PGE tailings material in Rustenburg. Minerals detected by MICA analysis of ASD Fieldspec data are highlighted in green. X-ray fluorescence analysis (XRF) data of selected trace elements from the PGE tailings material in Rustenburg.

Rustenburg		Minerals	V/ppm	Cr/%	Co/ppm	Ni/ppm
Tailings Location						
Spill Site	chromite, plagioclase, enstatite, montmorillonite, bronzite, chrysotile		1178	12.75	141	733
UG2 Tailings	chromite, plagioclase, enstatite, montmorillonite, bronzite		726	7.83	125	639
Merensky Tailings	chromite, plagioclase, enstatite, montmorillonite, bronzite		465	4.35	92	688

Figure 7. Iron feature depth (IFD) over the Rustenburg tailings complex calculated from OLI data overlain on the grayscale near-infrared (NIR) channel of OLI (a), directly below. USGS MICA Analysis from Hyperion data overlain on the gray-scaled NIR channel of OLI (b). Note the close match between the IFD in (a) and the iron-bearing minerals and cover types shown in (b) (bronzite, diopside and desert varnish).



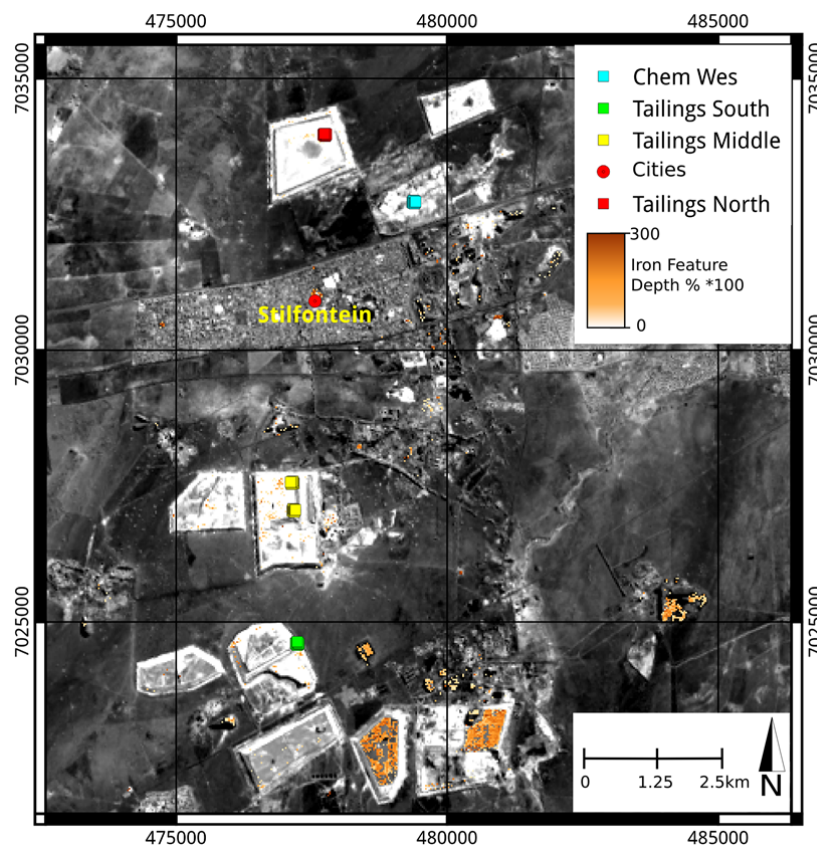
(a)



(b)

Figure 8a shows an example of IFD from OLI together with hyperspectral mineral analysis through USGS MICA from Hyperion data over Stilfontein in Figure 8b. Here, the link between the spatial extent of the IFD (Figure 8a) and the spatial distribution pattern of iron-bearing minerals (Figure 8b) is not as significant as in case of the PGE tailings near Rustenburg. This can be attributed to the smaller spectral contrast, due to the lower spatial abundance of iron-bearing minerals in the quartz-rich substrate of the milled conglomerate reefs. For example, the XRD analysis of Makhado [54], Table 3, from surface samples of the tailings dam in the north shows no prominent secondary iron-bearing mineral, whilst the analysis of the southern tailings and the Chem Wes area only shows the presence of jarosite, which is a possible indicator of AMD generation, according to Swayze *et al.* [1]. This may result in the liberation of potentially problematic trace elements, which are present in the tailings material, as shown in Table 3. Here, we find high concentrations of uranium (>400 ppm) and arsenic (200 ppm), as in case of the middle tailings.

Figure 8. Iron feature depth for the tailings areas near Klerksdorp (Stilfontein) calculated from OLI data and overlain on the grayscale NIR channel of OLI (a), directly below. Note the lesser spatial resemblance between the mica analysis in Figure (b) and the IFD image (a). USGS MICA analysis from Hyperion data for the tailings areas near Klerksdorp (Stilfontein) overlain on the gray-scaled NIR channel of OLI (b). The yellow box outlines an area that is affected by the presence of secondary iron minerals.



(a)

Figure 8. Cont.

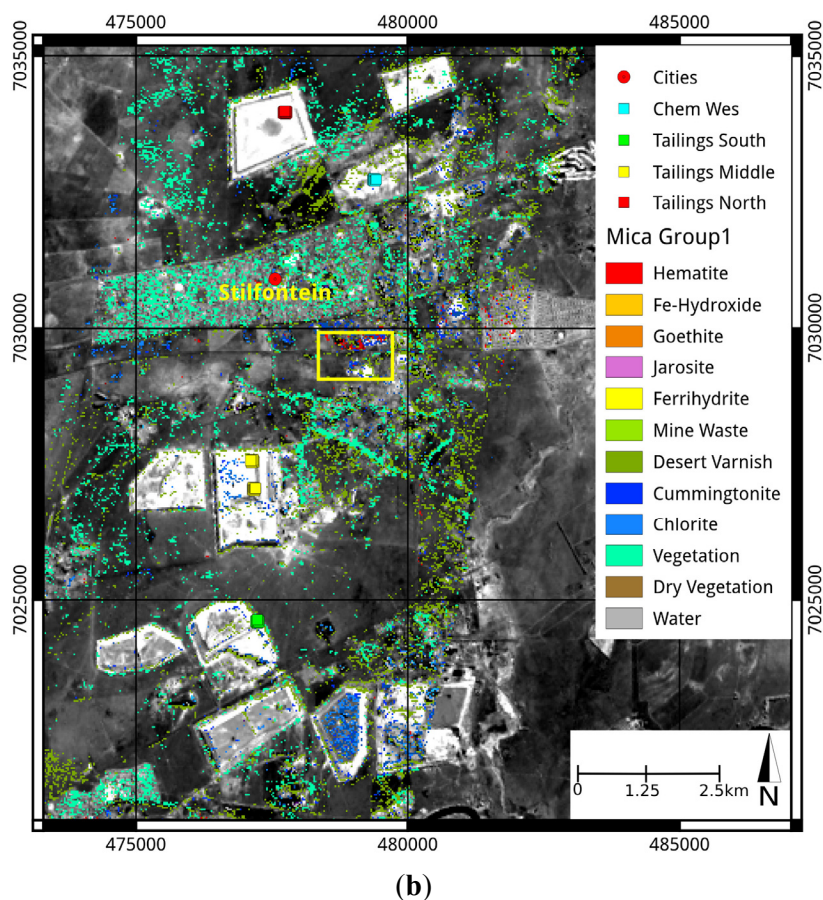


Table 3. Mineralogical data from X-ray diffraction analysis (XRD) of gold mine tailings samples, directly below. Minerals that have been found through MICA analysis of ASD Fieldspec data are highlighted in green. Selected trace elements (in ppm) from gold mine tailings, by X-ray fluorescence data (XRF) from tailings samples.

Stilfontein					
Tailings Location	Minerals	U/ppm	As/ppm	Pb/ppm	Th/ppm
Chem Wes Footprint	quartz, pyrophyllite, goethite, gypsum, jarosite, smectite, illite	90	91	79	35
Middle Tailings	quartz, pyrophyllite, goethite, gypsum, jarosite, smectite, illite	421	200	112	32
Northern Tailings	quartz, pyrophyllite, gypsum, smectite, uranopilite	154	106	131	21

Factors that may mask the iron absorption feature of gold tailings are crusts of gypsum that may form in environments with high evaporation rates, as shown in the XRD data and data from the MICA analysis of the ASD field spectra (Table 3). Additionally, clay minerals, as shown in the XRD analysis and in the MICA analysis of the field spectra, also tend to form covering blankets on tailings dams, as they are sedimented as the last mineral fraction after slurry deposition. Another important fact that determines the shape and depth of the absorption band and, hence, impacts on the IFD are grain size and the presence of other iron-bearing minerals [21]. The presence of organic matter is also able to mask the iron absorption band at 900 nm [55].

5.2. Iron Feature Depth in the Tailings Environment

The IFD calculation was done for validation purpose for the above discussed sensors from ASD field-spectroscopy data that was resampled to the spectral resolution of EnMAP, Sentinel-2, ALI, ASTER, OLI and ETM+. This was done for the platinum tailings, as shown in Figure 9, and for the gold mine tailings shown in Figure 10. In these figures, only the ability to map the magnitude of the IFD is compared in contrast to mapping the overall shape of the iron absorption feature, as shown in Figure 5a,b. Table 4 lists the root-mean-square error for the IFD values shown in Figures 9 and 10. Here, it becomes clear that the multispectral sensor ranking for the mapping of the IFD is as follows: Sentinel-2 shows the least deviation from the IFD calculated from EnMAP data, followed by ALI and OLI, whilst ETM+ and ASTER show the least performance for mapping the magnitude of the IFD. This is consistent with the results that have been discussed above and that are shown in Figure 5a,b.

Another interesting aspect is that IFD values from the PGE tailings material in Figure 9 are generally larger, due to the higher contrast of the 900 nm absorption feature when compared to gold tailings material. This fact is also shown in the spectra of Figure 4 and 6. An explanation for this could be found if the IFD values of the potential mineral components of these tailings facilities are calculated, shown in the Supplementary Materials. Here, Figures S3 and S4 were calculated from USGS library spectra [51]. Only jarosite shows comparable IFD values (<24%) to bronzite, a major mineral component of the PGE tailings material, whilst other, more common secondary iron minerals have IFDs of 18% and below. This also impacts the spatial distribution and magnitude of the IFD shown in Figure 7a and Figure 8a with the result that the potential spatial extent of PGE tailings material is more robustly mapped than the extent of gold tailings material, due to the high contrast of the iron absorption feature in the bronzite-bearing material.

Mixtures of different surface cover types, e.g., of vegetation and tailings material, show a significant impact on the IFD, as shown in Figure 11, where we see a decrease in IFD if vegetation cover increases. The Supplementary Materials show mixtures of PGE tailings material with vegetation. A growing proportion of vegetation on the test surface shallows the iron absorption feature and, therefore, decreases the IFD, until it is not detectable anymore.

Table 4. Root-mean-square error of iron feature depth calculated from resampled ASD field-spectroscopy data.

Sensor	RMSE of IFD, PGE Tailings	RMSE of IFD, Gold Tailings
Sentinel-2	0.015	0.017
ALI	0.020	0.026
ASTER	0.055	0.050
OLI	0.036	0.042
ETM+	0.046	0.046

Figure 9. Iron feature depth analysis of *in situ* ASD field-spectroscopy data from the PGE tailings material spectrally resampled to different multispectral sensors. The performance of the multispectral sensors is directly visible, with Sentinel-2 and ALI performing well compared to the weaker signal in the OLI data, whilst ASTER and ETM+ show the least resemblance to the EnMAP IFD.

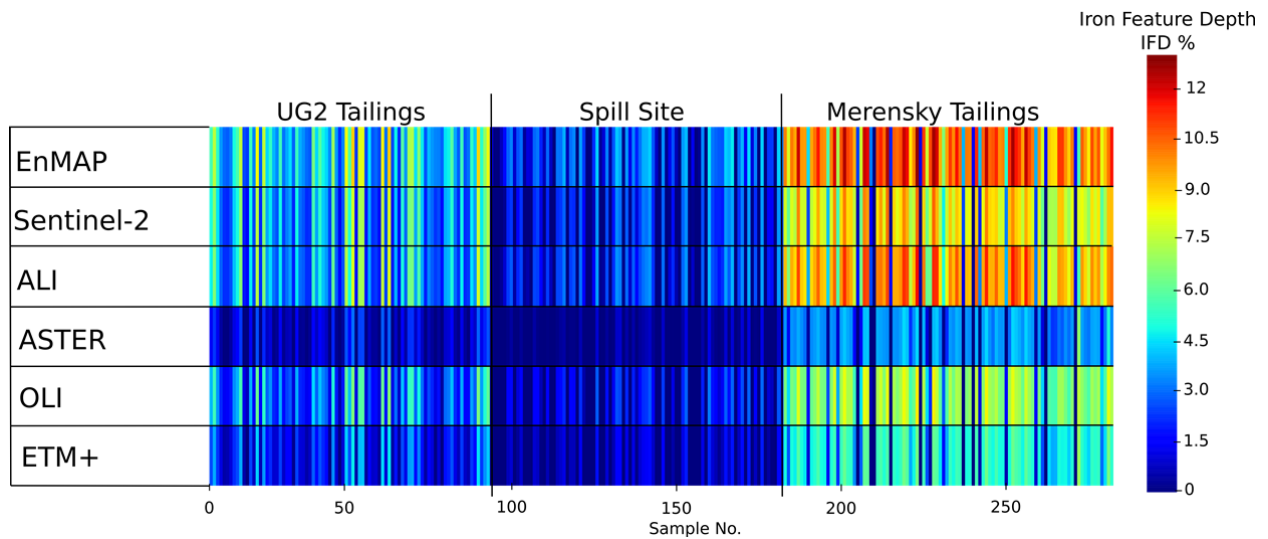


Figure 10. Iron feature depth analysis of *in situ* ASD field-spectroscopy data from gold mine tailings material spectrally resampled to different multispectral sensors. The performance of the multispectral sensors is directly visible, with Sentinel-2 and ALI performing well compared to the weaker signal in the OLI data, whilst ASTER and ETM+ show the least resemblance to the EnMAP IFD. The overall IFD values are generally lower, as in the case of the PGE tailings, due to the presence of secondary iron minerals only.

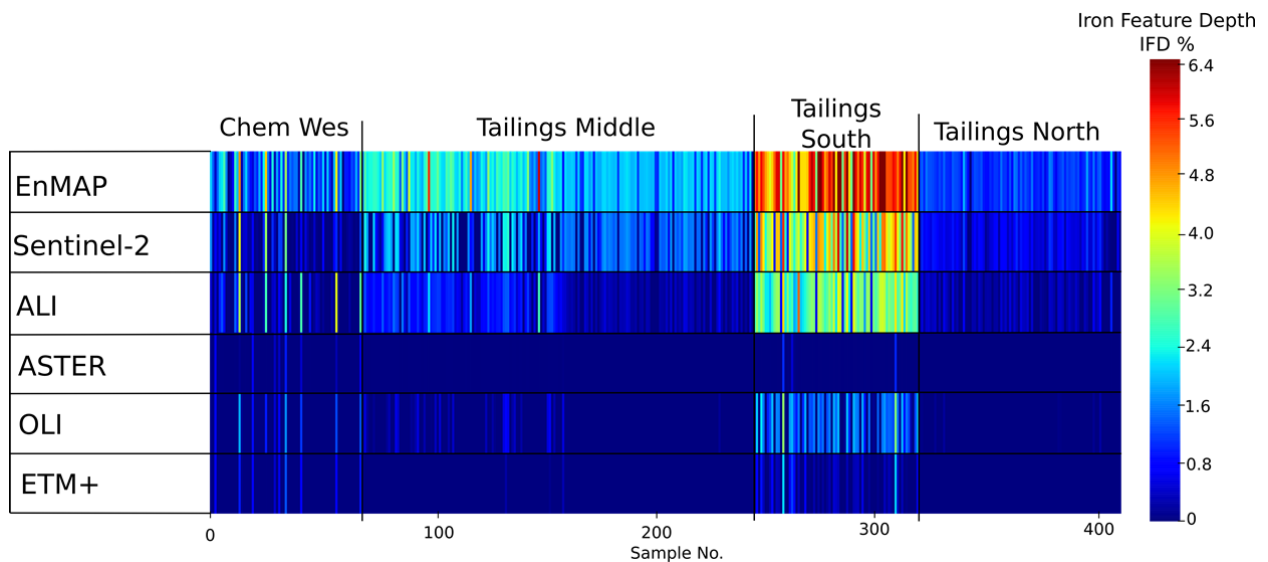
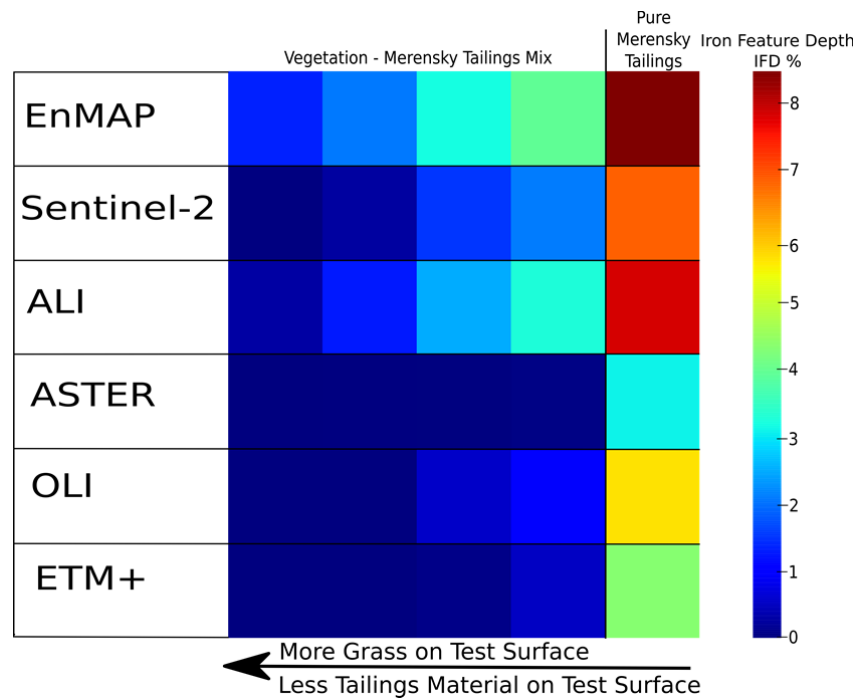


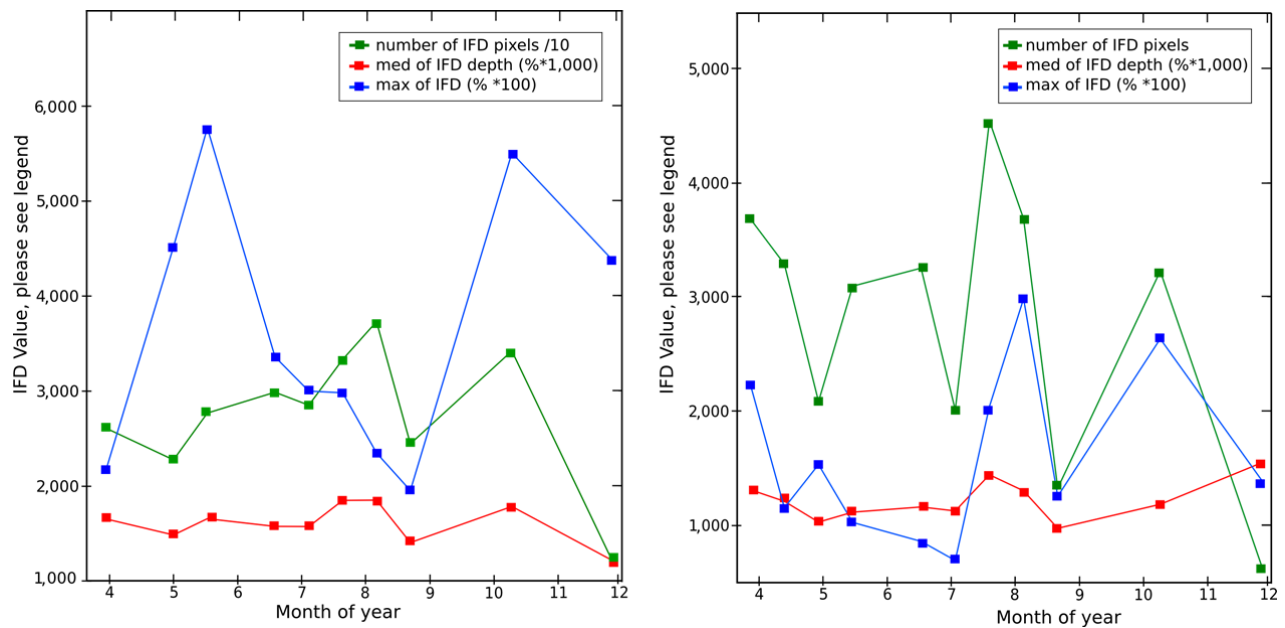
Figure 11. Iron feature depth analysis from *in situ* ASD field-spectroscopy data from PGE tailings material and mixtures of tailings material with vegetation.



5.3. Multi-Temporal Analysis

For an additional analysis step, spatial information can be extracted from a multi-temporal analysis of the IFD and its distribution across the tailings areas of interest. This represents an important step towards the monitoring of tailings and mine waste areas and their spatial extent. Figure 12 shows multi-temporal IFD data for Rustenburg and for the tailings near Stilfontein calculated from Landsat-8 OLI data. It is clear that a large number of pixels with significant IFD are mapped during the dry season in the South African winter, when the dry vegetation is not masking the iron absorption feature, as discussed above. The highest IFD values in Figure 12 have been detected during autumn and spring, the months with the greatest precipitation, when moisture is available, and can facilitate the generation of secondary iron minerals and crusts, due to the enhanced weathering of primary iron-bearing minerals, such as pyrite. The opposite trend of maximum IFD and dry season in the case of the platinum tailings could have been caused by a larger spatial abundance of evaporation crusts on the tailings dams, which might mute the strong IFD signal of the pyroxenes. It is important to continue with the analysis presented in Figure 12 in the next two years to achieve a more robust result and to validate the variability found in the IFD data, as standard Level 1 OLI data is only available from the start of the mission in March 2013. This will show if the trends and variability observed in Figure 12 can be linked to annual changes in the weather pattern or other external factors.

Figure 12. Multi-temporal iron feature depth (IFD) data from the tailings facilities near GaLuka, Rustenburg (**left**) and from the tailings in Stilfontein (**right**), calculated from the multispectral OLI data scenes listed in Table A1. The high number of IFD pixels in the dry season, July–September, could be attributed to sparser vegetation cover during that time. Please note that the trend in the number of IFD pixels in Rustenburg (left) is similar to the trend in the number of IFD pixels in Klerksdorp (right). A similar observation can be made for the median of the IFD depth between the two sites.



6. Conclusion and Outlook

It was shown that Multispectral data is suitable for mapping the spatial extent of iron minerals that are part of mine waste material via a new absorption feature-based index, which we call the iron feature depth.

Through laboratory work with mine waste samples and PSF adapted field sampling, the following quantitative multispectral sensor rankings were established that illustrate the sensors capabilities to describe mine waste through the 900-nm iron absorption feature. For spectra from gold mining material, the ranking is in descending order as follows: EnMAP 100% similarity to the reference feature, ALI 97.5%, Sentinel-2 97%, OLI and ASTER 95% and ETM+ 91% similarity. If pyroxenes as proxies for platinum tailings material need to be mapped, the following similarity ranking applies: EnMAP 100% similarity to the reference, Sentinel-2 92%, OLI and ALI 89%, ASTER 82% and ETM+ 75% similarity. Thus, the mean accuracy for mapping the 900-nm iron absorption feature of minerals related to mine waste is: EnMAP 100%, Sentinel-2 94.5%, ALI 93.25%, OLI 92%, ASTER 88.5% and ETM+ 83%. This sensor ranking is consistent with the RMSE of the IFD in Table 4.

However, only hyperspectral data is able to discriminate surface mineralogy correctly, as shown in Figures 7a,b and 8a,b, and provides an independent verification of the spatial distribution of mine waste material and, henceforth, shows the geoscientific relevance of multispectral data and the IFD for mapping the spatial extent of mine waste. In addition to this, we have seen that hyperspectral

data is necessary if the IFD is to be calculated for mixed surface cover types, such as vegetation and tailings material. Current multispectral sensors are not able to address this problem, as shown in the Supplementary Materials. Only next generation multispectral sensors, such as Sentinel-2, are better equipped for this task.

Hyperspectral data shows its superiority over any of the considered multispectral instruments if the IFD is to be calculated for mixed pixels with a notable percentage of vegetation cover in the pixel. Here, only EnMAP is able to determine the IFD of mixed tailings and vegetation spectra.

Sentinel-2 and EnMAP might, therefore, in the future, be used as two primary building blocks of a multi-sensor process chain that helps to save costs in the remediation of mining sites. Such an application could become crucial for developing countries, such as Brazil or South Africa. Future studies should therefore focus on exploring those synergies between Sentinel-2 and EnMAP better. This could either be done using simulated data or the already available sensor systems of NASA, such as OLI/ALI and Hyperion.

Research questions that may be important for future studies are as follows:

- (1) What is the ideal band layout of a multispectral sensor that enables highly precise mine waste mapping?
- (2) What is the impact of spatial resolution on IFD mapping if, e.g., high spectrally and spatially-resolved airborne sensors are used in such a study to complement spaceborne data?
- (3) How are IFD and the spectral contrast of the surface types/minerals present related to each other?
- (4) Could the IFD serve as an exploration tool in addition to monitoring the extent of primary and secondary iron minerals on tailings surfaces?

Acknowledgments

We are indebted to USGS, NASA, Stuart Frye and the EO-1 Science Team for kindly providing recent Hyperion and ALI data. Landsat 8 and Landsat 7 data was kindly provided by the USGS through the Earth Explorer Platform. We thank UFS honours students Tendani Makhado and Leslie Reid for the mineralogical and geochemical analysis of our tailings samples as part of their honours project. This study was financed by the German National EnMAP framework program (Department of Economics and Technology BMWi No. 50EE1256). The authors would also like to thank the four anonymous reviewers for their careful work in enhancing the quality of this paper.

This is AEON contribution number 121; and Inkaba yeAfrica Contribution Number 93.

Conflict of Interest

We, the authors, state that we do not have any potential conflict of interest in presenting this work here.

Authors Contributions

Maarten de Wit and Hermann Kaufmann generously provided the infrastructure and the funding for this work, including fieldwork and spectral laboratory analysis equipment. Christoph Gauert kindly

provided critical geochemical analysis of the surface samples and a review of the XRF and XRD data acquired by his B.Sc. Honours students Tendani Makhado and Leslie Reid. Christian Rogass provided critical assistance with the image processing, providing the in-house HySpex pre-processing program. His comments to the manuscript as well as his remarks to the main image processing source-code from Christian Mielke made this work possible. Special thanks to Nina Boesche for the geological input and feedback on tailings sites and field results and for the critical review of this manuscript. Christian Mielke developed and tested the sensor adopted Iron Feature Depth index, carried out the fieldwork, the hyperspectral laboratory analysis and the associated programming and preprocessing work.

References

1. Swayze, G.A.; Smith, K.S.; Clark, R.N.; Sutley, S.J.; Pearson, R.M.; Vance, J.S.; Hageman, P.L.; Briggs, P.H.; Meier, A.L.; Singleton, M.J.; *et al.* Using imaging spectroscopy to map acidic mine waste. *Environ. Sci. Technol.* **2000**, *34*, 47–54.
2. Montero S., I.C.; Brimhall, G.H.; Alpers, C.N.; Swayze, G.A. Characterization of waste rock associated with acid drainage at the Penn Mine, California, by ground-based visible to short-wave infrared reflectance spectroscopy assisted by digital mapping. *Chem. Geol.* **2005**, *215*, 453–472.
3. Riaza, A.; Buzzi, J.; García-Meléndez, E.; Vázquez, I.; Bellido, E.; Carrère, V.; Müller, A. Pyrite mine waste and water mapping using Hymap and Hyperion hyperspectral data. *Environ. Earth Sci.* **2012**, *66*, 1957–1971.
4. Choe, E.; van der Meer, F.; van Ruitenbeek, F.; van der Werff, H.; de Smeth, B.; Kim, K.W. Mapping of heavy metal pollution in stream sediments using combined geochemistry, field spectroscopy, and hyperspectral remote sensing: A case study of the Rodalquilar mining area, SE Spain. *Remote Sens. Environ.* **2008**, *112*, 3222–3233.
5. Fischer, C.; Busch, W. Monitoring of environmental changes caused by hard-coal mining. *Proc. SPIE* **2002**, *4545*, 64–72.
6. Kopačková, V.; Chevrel, S.; Bourguignon, A.; Rojik, P. Application of high altitude and ground-based spectroradiometry to mapping hazardous low-pH material derived from the Sokolov open-pit mine. *J. Maps* **2012**, *8*, 220–230.
7. Kopačková, V. Using multiple spectral feature analysis for quantitative pH mapping in a mining environment. *Int. J. Appl. Earth Obs. Geoinf.* **2014**, *28*, 28–42.
8. Richter, N.; Staenz, K.; Kaufmann, H. Spectral unmixing of airborne hyperspectral data for baseline mapping of mine tailings areas. *Int. J. Remote Sens.* **2008**, *29*, 3937–3956.
9. Debba, P.; Carranza, E.J.M.; Stein, A.; van der Meer, F.D. Optimum Sampling Scheme for Characterization of Mine Tailings. In Proceedings of 2009 IEEE International Geoscience and Remote Sensing Symposium, Cape Town, South Africa, 21–27 July 2009; Volume 4, pp. 897–900.
10. Murphy, R.J.; Monteiro, S.T. Mapping the distribution of ferric iron minerals on a vertical mine face using derivative analysis of hyperspectral imagery (430–970 nm). *ISPRS J. Photogramm. Remote Sens.* **2013**, *75*, 29–39.

11. McCarthy, T.S.; Steyl, G.; Maree, J.; Zhao, B.; Ramontja, T.; Coetzee, H.; Hobbs, P.J.; Burgess, J.E.; Thomas, A.; Keet, M.; *et al.* *Mine Water Management in the Witwatersrand Gold Fields with Special Emphasis on Acid Mine Drainage*; Department of Water Affairs, South Africa: Johannesburg, South Africa, 2010; p. 146.
12. Harrison, S.; Broadhurst, J.; van Hille, R.; Oyekola, O.; Hesketh, B.C.; Opitz, A.A. *A Systematic Approach to Sulphidic Waste Rock and Tailings Management to Minimise Acid Rock Drainage Formation: Report to the Water Research Commission*; Water Research Commission: Pretoria, South Africa, 2010.
13. Coetzee, H. Acid Mine Drainage in South Africa: Applications of EO Products and the EO-Miners Experience. In Proceedings of EO-MINERS Final Scientific and Technical Conference, Versailles, France, 10–11 October 2013.
14. Ungar, S.G.; Pearlman, J.S.; Mendenhall, J.A.; Reuter, D. Overview of the Earth Observing One (EO-1) mission. *IEEE Trans. Geosci. Remote Sens.* **2003**, *41*, 1149–1159.
15. Thome, K.J.; Biggar, S.F.; Wisniewski, W. Cross comparison of EO-1 sensors and other Earth resources sensors to Landsat-7 ETM+ using Railroad Valley Playa. *IEEE Trans. Geosci. Remote Sens.* **2003**, *41*, 1180–1188.
16. Irons, J.R.; Dwyer, J.L.; Barsi, J.A. The next Landsat satellite: The Landsat Data Continuity Mission. *Remote Sens. Environ.* **2012**, *122*, 11–21.
17. Kaufmann, H.; Segl, K.; Guanter, L.; Hofer, S.; Foerster, K.P.; Stuffer, T.; Mueller, A.; Richter, R.; Bach, H.; Hostert, P.; *et al.* Environmental Mapping and Analysis Program (EnMAP)—Recent Advances and Status. In Proceedings of IEEE International Geoscience and Remote Sensing Symposium, Boston, MA, USA, 7–11 July 2008; Vol. 4, pp. 109–112.
18. Drusch, M.; Del Bello, U.; Carlier, S.; Colin, O.; Fernandez, V.; Gascon, F.; Hoersch, B.; Isola, C.; Laberinti, P.; Martimort, P. *et al.* Sentinel-2: ESA's Optical High-Resolution Mission for GMES Operational Services. *Remote Sens. Environ.* **2012**, *120*, 25–36.
19. Singer, R.B. Near-infrared spectral reflectance of mineral mixtures: Systematic combinations of pyroxenes, olivine, and iron oxides. *J. Geophys. Res.: Solid Earth* **1981**, *86*, 7967–7982.
20. Murphy, R.J.; Schneider, S.; Monteiro, S.T. Consistency of measurements of wavelength position from hyperspectral imagery: Use of the ferric iron crystal field absorption at ~ 900 nm as an indicator of mineralogy. *IEEE Trans. Geosci. Remote Sens.* **2014**, *52*, 2843–2857.
21. Townsend, T.E. Discrimination of iron alteration minerals in visible and near-infrared reflectance data. *J. Geophys. Res.: Solid Earth* **1987**, *92*, 1441–1454.
22. Hunt, G.R.; Ashley, R.P. Spectra of altered rocks in the visible and near infrared. *Econ. Geol.* **1979**, *74*, 1613–1629.
23. Frimmel, H.E.; Minter, W.E.L. Recent developments concerning the geological history and genesis of the Witwatersrand gold deposits, South Africa. In *Integrated Methods for Discovery: Global Exploration in the Twenty-First Century*; Goldfarb, R.J., Nielsen, R.L., Eds.; Special Publication Society of Economic Geologists: Littleton, CO, USA, 2002; Volume 9, pp. 17–45.
24. Hayward, C.L.; Reimold, W.U.; Gibson, R.L.; Robb, L.J. Gold mineralization within the Witwatersrand Basin, South Africa: evidence for a modified placer origin, and the role of the Vredefort impact event. *Geol. Soc. Lond. Spec. Publ.* **2005**, *248*, 31–58.

25. Scoates, J.S.; Friedman, R.M. Precise age of the Platiniferous Merensky Reef, bushveld complex, South Africa, by the U-Pb Zircon Chemical Abrasion ID-TIMS technique. *Econ. Geol.* **2008**, *103*, 465–471.
26. Mondal, S.K.; Mathez, E.A. Origin of the UG2 chromitite layer, Bushveld Complex. *J. Petrol.* **2007**, *48*, 495–510.
27. Blight, G.E.; Robinson, M.J.; Diering, J.A. C. The flow of slurry from a breached tailings dam. *J. South Afr. Inst. Min. Metall.* **1981**, *81*, 1–8.
28. Bosch, D.W. Retreatment of residues and waste rock. *Extr. Metall. Gold South Afr.* **1987**, *2*, 707–743.
29. Mielke, C.; Fuchs, Y.; Rogass, C.; Segl, K.; Pustlauck, F.; Blumenstein, O.; Kaufmann, H.; de Wit, M. The Potential of Spectroscopy to Monitor Mine Waste and Acid Mine Drainage in South Africa. In Proceedings of 4th EARSeL Workshop on Remote Sensing and Geology, Mykonos Island, Greece, 24–25 May 2012.
30. Van der Meer, F.D.; van der Werff, H.; van Ruitenbeek, F.J.A.; Hecker, C.A.; Bakker, W.H.; Noomen, M.F.; van der Meijde, M.; Carranza, E.J.M.; Smeth, J.; Woldai, T. Multi- and hyperspectral geologic remote sensing: A review. *Int. J. Appl. Earth Obs. Geoinf.* **2012**, *14*, 112–128.
31. Sabins, F.F. Remote sensing for mineral exploration. *Ore Geol. Rev.* **1999**, *14*, 157–183.
32. Heinrich, V.; Krauss, G.; Goetze, C.; Sandow, C. IDB—Index DataBase. Available online: <http://www.indexdatabase.de/> (accessed on 17 April 2014).
33. Richter, R.; Schläpfer, D. *Atmospheric/Topographic Correction for Satellite Imagery; ATCOR-2/3 User Guide Version; ReSe Applications Schläpfer: Wil, Switzerland, 2012*; p. 203.
34. Wang, Z.; Bovik, A.C.; Sheikh, H.R.; Simoncelli, E.P. Image quality assessment: From error visibility to structural similarity. *IEEE Trans. Image Process.* **2004**, *13*, 600–612.
35. Van der Walt, S.; Schoenberger, J.L.; Nunez-Iglesias, J.; Boulouge, F.; Warner, J.D.; Yager, N.; Gouillart, E.; Yu, T. scikit-image: Image processing in Python. *PeerJ* **2014**, *2*, e453. Available online: <https://peerj.com/preprints/336v2/> (accessed on 17 April 2014).
36. Clark, R.N.; Swayze, G.A.; Livo, K.E.; Kokaly, R.F.; Sutley, S.J.; Dalton, J.B.; McDougal, R.R.; Gent, C.A. Imaging spectroscopy: Earth and planetary remote sensing with the USGS Tetracorder and expert systems. *J. Geophys. Res.: Planets* **2003**, *108*, 5–1–5–44.
37. Rowan, L.C.; Mars, J.C. Lithologic mapping in the Mountain Pass, California area using Advanced Spaceborne Thermal Emission and Reflection Radiometer (ASTER) data. *Remote Sens. Environ.* **2003**, *84*, 350–366.
38. Kalinowski, A.; Oliver, S. *ASTER Mineral Index Processing Manual*; Australian Government Publication; Remote Sensing Applications, Geoscience Australia: Symonston, ACT, Australia, 2004; p. 37.
39. Volesky, J.C.; Stern, R.J.; Johnson, P.R. Geological control of massive sulfide mineralization in the Neoproterozoic Wadi Bidah shear zone, southwestern Saudi Arabia, inferences from orbital remote sensing and field studies. *Precambrian Res.* **2003**, *123*, 235–247.
40. Bannari, A.; Morin, D.; Bonn, F.; Huete, A.R. A review of vegetation indices. *Remote Sens. Rev.* **1995**, *13*, 95–120.

41. Datt, B.; McVicar, T.R.; Van Niel, T.G.; Jupp, D.L.B.; Pearlman, J.S. Preprocessing EO-1 Hyperion hyperspectral data to support the application of agricultural indexes. *IEEE Trans. Geosci. Remote Sens.* **2003**, *41*, 1246–1259.
42. Staenz, K.; Neville, R.A.; Clavette, S.; Landry, R.; White, H.P.; Hitchcock, R. Retrieval of Surface Reflectance from Hyperion Radiance Data. In Proceedings of 2002 IEEE International Geoscience and Remote Sensing Symposium, Toronto, ON, Canada, 24–28 June 2002; Volume 3, pp. 1419–1421.
43. Kokaly, R.F. Spectroscopic remote sensing for material identification, vegetation characterization, and mapping. *Proc. SPIE* **2012**, *8390*, doi:10.1117/12.919121.
44. Rabe, A.; Jakimov, B.; Held, M.; van der Linden, S.; Hostert, P. EnMAP-Box. Available online: http://www.enmap.org/?q=box_download (accessed on 17 April 2014).
45. Baarstad, I.; Løke, T.; Kaspersen, P. ASI—A New Airborne Hyperspectral Imager. In Proceedings of the 4th EARSeL Workshop on Imaging Spectroscopy—New Quality in Environmental Studies, Warsaw, Poland, 26–29 April 2005.
46. Xie, H.; Hicks, N.; Keller, G.R.; Huang, H.; Kreinovich, V. An IDL/ENVI implementation of the FFT-based algorithm for automatic image registration. *Comput. Geosci.* **2003**, *29*, 1045–1055.
47. Abrams, M. The Advanced Spaceborne Thermal Emission and Reflection Radiometer (ASTER): Data products for the high spatial resolution imager on NASA's Terra platform. *Int. J. Remote Sens.* **2000**, *21*, 847–859.
48. Boggs, T. Spectral Python (SPy)—Spectral Python 0.14 Documentation. Available online: <http://www.spectralpython.net/> (accessed on 17 April 2014).
49. Segl, K.; Guanter, L.; Rogass, C.; Kuester, T.; Roessner, S.; Kaufmann, H.; Sang, B.; Mogulsky, V.; Hofer, S. EeteS—The EnMAP end-to-end simulation tool. *IEEE J. Sel. Top. Appl. Earth Obs. Remote Sens.* **2012**, *5*, 522–530.
50. Keef, J.L. Hyper-spectral Sensor Calibration Extrapolated from Multi-Spectral Measurements. Ph.D. Thesis, University of Arizona, Tucson, AZ, USA, 2008.
51. Clark, R.N.; Swayze, G.A.; Wise, R.; Livo, E.; Hoefen, T.M.; Kokaly, R.F.; Sutley, S.J. *USGS Digital Spectral Library splib06a*; Clark, Ed.; U.S. Geological Survey Data Series; Digital Data Series 231; U.S. Geological Survey: Denver, CO, USA, 2007.
52. *Handbook of Mineralogy*; Anthony, J.W.; Bideaux, R.A.; Bladh, K.W.; Nichols, M.C., Eds.; Mineralogical Society of America: Chantilly, VA, USA, 2004.
53. Reid, L. Mineralogy and Geochemistry of Mine Dump, Tailings Site and Pipeline Spillage Samples from Impala Platinum Mine in Rustenburg. B.Sc. Thesis, Geology Department, University of the Free State, Bloemfontein, South Africa, 2012; unpublished.
54. Makhado, T.C. Mineralogy and Geochemistry of Mine Dump, Tailings Site Samples from the Stilfontein Gold Mining Site. B.Sc. Thesis, Geology Department, University of the Free State, Bloemfontein, South Africa, 2012; unpublished.
55. Galvao, L.S.; Vitorello, I. Role of organic matter in obliterating the effects of iron on spectral reflectance and colour of Brazilian tropical soils. *Int. J. Remote Sens.* **1998**, *19*, 1969–1979.

Appendix

Data References

Due to the larger number of used Landsat 8 scenes and sensor data from ALI, Hyperion and ETM+, the data is referenced in this specific chapter. Table A1 shows the Landsat 8 data used in this study. Scene IDs of the ALI and Hyperion data used for the Rustenburg area are EO1A1710772013195110KF for ALI and EO1H1710772013195110KF for Hyperion. Scene IDs of the ALI and Hyperion data used for the Stilfontein area near Klerksdorp are EO1A1710782013271110KF for ALI and EO1H1710782013271110KF for Hyperion. Landsat 7 data used for the Klerksdorp area is L71171079_07920000516. Landsat 7 data used for the Rustenburg area is L71171078_07820010111.

Table A1. Landsat-8 Data used in this study.

Landsat 8 Scene IDs for Klerksdorp/Stilfontein	Landsat 8 Scene IDs for Rustenburg
LC81710792013116LGN01_QB	LC81710782013228LGN00_QB
LC81710792013132LGN01_QB	LC81710782013116LGN01_QB
LC81710792013148LGN00_QB	LC81710782013148LGN00_QB
LC81710792013164LGN00_QB	LC81710782013164LGN00_QB
LC81710792013196LGN00_QB	LC81710782013196LGN00_QB
LC81710792013212LGN00_QB	LC81710782013212LGN00_QB
LC81710792013228LGN00_QB	LC81710782013244LGN00_QB
LC81710792013244LGN00_QB	LC81710782013260LGN00_QB
LC81710792013260LGN00_QB	LC81710782013308LGN00_QB
LC81710792013308LGN00_QB	LC81710782013356LGN00_QB
LC81710792013356LGN00_QB	

© 2014 by the authors; licensee MDPI, Basel, Switzerland. This article is an open access article distributed under the terms and conditions of the Creative Commons Attribution license (<http://creativecommons.org/licenses/by/3.0/>).